

## Characterization of 3D Printed Fracture Networks

Anna Suzuki<sup>1</sup>, Stock Sawasdee<sup>1</sup>, Hiroshi Makita<sup>2</sup>, Toshiyuki Hashida<sup>2</sup>, Kewen Li<sup>1</sup> and Roland N. Horne<sup>1</sup>

<sup>1</sup> 367 Panama St, Stanford, CA 94305, USA

<sup>2</sup> 7-7-11-707 Aramaki-Aza-Aoba, Aoba-ku, Sendai, Miyagi 980-8579, JAPAN

anna3@stanford.edu

**Keywords:** tracer test, particle tracking, 3D printer, non-Fickian diffusion, fractal dimension

### ABSTRACT

Tracer testing has been used to obtain hydraulic properties in a reservoir system and may help characterize the fracture networks inside the reservoir. Numerous studies at various scales have shown that the distribution of many fracture properties (i.e., length, displacement) follows a power law scaling with some cutoffs. Fractal dimension is useful to evaluate the geometric characteristics of fracture networks. We studied mass transport in a fracture network where fracture lengths are given by a power law with maximum and minimum length. Effects of fractal dimension of fracture lengths on mass transport were investigated by particle tracking simulations and laboratory flow experiments in a fractured flow model. The numerical simulation results indicate that the fractal nature of the fracture length results in non-Fickian behavior on tracer responses. In the laboratory flow experiments, a 3D printer was used to create artificial fracture network models with different fractal dimensions. The experimental tracer responses of the 3D printed fracture model show similar features to the results by numerical simulation. A challenge of the printing process was the limited resolution of the 3D printer and the solubility of the supporting wax.

### 1. INTRODUCTION

Understanding of fracture networks and fluid flow within fractured rocks are essential problems for geothermal engineering. Various deterministic and probabilistic techniques have been developed in order to describe heterogeneous characteristics of fluid flow (Neuman, 2005). Most of these techniques require incorporating many input parameters (e.g., fracture properties in discrete fracture network models) and involve time-consuming statistical treatment. In addition, fractures within a reservoir are not directly accessible, in other words, the fracture properties can only be measured at their intersections with boreholes or outcrops. This forces geoscientists and reservoir engineers to construct reservoir models with high uncertainty and to depend on their subjectivity. In order to obtain direct information from the fluid flow, tracer testing has been used, which may help characterize the fracture networks within the reservoir. In this study, our goal was to characterize intrinsic complexity of fracture networks by using tracer response data from numerical and laboratory models.

Early works to study fracture systems are spread through a wide range of scales from core through outcrop to aerial photographs and satellite image scales. Their scaling attributes have received increasing attention motivated by a promise of statistical prediction. Understanding of the scaling characteristics of fracture networks will guide both the interpretation of regional data and its extrapolation to other different scales. Numerous studies at various scales have shown that the distribution of many fracture properties (i.e., length, displacement) follows a power-law scaling. Fractal geometry is in many cases well suited to describe objects that exhibit scaling behaviors. Fractal dimension can be measured on logarithmic plots and is useful to evaluate the geometric characteristics of fracture networks (e.g., Bour and Davy, 1997; Bonnet et al., 2001; Stigsson et al., 2001; Gustafson and Fransson, 2005). However, the problem of fractal geometry is the lack of any homogenization scale. In nature, power laws scaling must have upper and lower cutoffs. Physical length scales in the system provided by discontinuous structures (i.e., lithological layering, fault zone size, etc.) can give rise to limits to the scale range over which the fractal geometry is valid (Odling et al., 1999).

Nonetheless, mathematical concept of fractal (or power-law scaling) is very attractive because it can be extended to develop so-called nonlocal models based on fractional calculus and fractional-order differential equations. The nonlocal models have been a subject of interest not only among mathematicians but also among physicists and engineers. Indeed, we can find numerous applications in porous media, electrochemistry, electromagnetism, signal processing, dynamics of earthquakes, biosciences, medicine, economics, probability and statistics, astrophysics, chemical engineering, physics, bioengineering, fluid mechanics, thermodynamics, neural networks, etc. (e.g., Mainardi, 1997; Diethelm and Freed, 1999; Hilfer, 2000; Magin, 2006; Tarasov, 2010; Sheng et al., 2011; Sabatier et al., Abbas et al., 2012). In hydrology, anomalous tracer transport in heterogeneous media has been observed, which can be modeled by the nonlocal mass transport equations (e.g., the Multi-Rate Mass Transfer (MRMT) model (Haggerty and Gorelick, 1995), the Continuous Time Random Walk (CTRW) framework (Berkowitz et al., 2006), and the Fractional-Derivative Model (Baeumer and Meerschaert, 2010; Benson, 1998; Huang et al., 2006; Zhang et al., 2009a). Schumer et al. (2003) proposed a fractal mobile/immobile model for solute transport. The model includes fractal (power law) distribution of rate coefficients that is scale invariant in time and leads to a term including temporal fractional derivative in the transport equation. Assuming that a fractured medium consists of porous media that follow fractal scaling (e.g., pore sizes varying in a wide range of scale), the fractional-order differential equations can describe the anomalous transport in a fractured medium (Fomin et al., 2011). Several applications in natural and experimental systems have shown that the nonlocal models can be candidates to quantify anomalous transport in heterogeneous systems (e.g., Benson et al., 2001, 2000a, 2000b; Haggerty et al., 2002; Schumer et al., 2003).

If the nonlocal models and the fractal concepts (power law scaling) can compensate the lack between the mathematical theories and the geophysical processes including upper and/or lower thresholds, the models would provide reasonable and realistic characterization of heterogeneous fracture distribution. Truncated stable Levy flights were proposed by Mantegna and Stanley (1994) to censor arbitrarily large jumps, and capture the natural cutoff in real physical systems. Exponentially tempered stable processes were proposed by Carlea and del-Castillo-Negrete (2007) and Rosin'ski (2007) as a smoother alternative, without a sharp cutoff. Meerschaert et al. (2008) proposed the tempered anomalous diffusion model containing both the classical mass transport model and the temporal fractional derivative model as end members. Experimental and numerical investigation indicates that the temporal fractional derivative model captures mass transport in an ideal fractal medium, while the tempered anomalous diffusion model can capture an upper truncated tracer behavior in a system containing a discontinuous structure (Suzuki et al., 2016). Using such truncated models might help provide description of truncated mass transport beyond the fractal theory and are expected to contribute to broad application in real physical systems.

We studied mass transport in a fracture network where fracture lengths are given by a power law with cutoffs. Effects of fractal dimension of fracture lengths on mass transport are discussed. It has been generally recognized that field observations at outcrops or in core samples measure fractures incompletely (Einstein and Baecher, 1983; Segall and Pollard, 1983). Short fractures are incompletely observed because of the limit of image resolution, while long fractures exceed the observed area. The resolution and censoring effects result in altering the appearance of the distribution. In order to investigate thresholds of inherent fracture distributions, it is necessary to distinguish truncation effects that are caused by measurement resolution. Therefore, this study used fracture distributions where the upper and the lower limits of fractures can be controlled. Numerical simulation and laboratory experiment were conducted. Samples of fracture networks were created using a 3D printer for the laboratory flow experiments.

## 2. THEORY

### 2.1 Scaling of fracture systems

Numerous studies of fracture system scaling in the literature suggest that scaling laws exist in nature. Fractal geometry is in many cases well suited to the description of objects that exhibit scaling behavior. The mathematical theory of fractals is described by Mandelbrot (1982), and more information about fractals is given by Feder (1988), Falconer (1990), and Vicsek (1992). The fractal dimension does not completely define the geometry of the fracture system, and a complete characterization should include various geometrical attributes such as density, length, orientation, roughness of the fracture surface, width, aperture, shear displacement, etc.

From the study of natural fractures datasets (Castaing et al., 1996; Odling et al., 1999; Le Garzic et al., 2011), fracture length distributions are characterized using log-log diagrams where the cumulative frequency distribution  $N(r)$  (number of fractures with length greater or equal to size  $r$ ) is plot versus radius  $r$  and follows a power law as

$$N(r) = Cr^{-D_R}, \quad (1)$$

where  $C$  is a constant characteristic to describe fracture density.  $D_R$  is the power-law exponent (Bour and Davy, 1997; Odling, 1997), which presents fractal dimension of fracture length. The power-law exponent characterizes relative abundance of fractures with different sizes. Small fractures dominate the connectivity when  $D_R$  is larger, while the connectivity is influenced by the large fractures with smaller  $D_R$  (Le Garzic et al., 2011). When the upper and lower size limits are given, the number of fracture can be written as

$$N = C [r_{min}^{-D_R} - r_{max}^{-D_R}], \quad (2)$$

where  $r_{min}$  and  $r_{max}$  are the minimum and maximum radius of fractures, respectively. Consider some fraction of this total number counting from  $r_{max}$  upward and the corresponding size  $r_\alpha$  of the largest object in that fraction. Eq. (2) can be rewritten as

$$N = \alpha N = \alpha C [r_{min}^{-D_R} - r_{max}^{-D_R}] = C [r_{min}^{-D_R} - r_\alpha^{-D_R}]. \quad (3)$$

From Eqs. (2) and (3), we obtain

$$N = [(1 - \alpha) r_{min}^{-D_R} + \alpha r_{max}^{-D_R}]^{-1/D_R}, \quad (4)$$

which gives an expression for the radius of a random fractal drawn from a truncated fractal distribution of fractal dimension  $D_R$  where  $\alpha$  is a uniform deviate on  $[0, 1]$ .

### 2.2 Mass transport in fractal media

Elementary particles under an effect of different force fields of different nature perform complex motion. The trajectories of these particles reproduce geometrical objects of complex fractal structure (Shlesinger, 1993). Diffusion in the media of fractal geometry was investigated extensively in last three decades (O'Shaughnessy and Procaccia, 1985; Giona and Roman, 1992; Schumer et al., 2003).

There are some approaches for describing diffusion in fractal media. The first approach uses a diffusion coefficient as a function of spatial coordinates and describes probability of particles appearing at some point of medium at given moment of time  $t$ . We can define a diffusion coefficient as:

$$D(x) = D_0 x^{-\theta}, \quad (5)$$

where  $D_0$  is a constant and  $x$  is scale of the object, it leads to the following diffusion equation:

$$\frac{\partial C}{\partial t} = \frac{\partial}{\partial x} \left( D_0 x^{-\theta} \frac{\partial C}{\partial x} \right) \quad (6)$$

When the particle movement follows the classical Fick's law, the standard deviation of the motion can be written as  $\sigma = (Dt)^{1/2}$ , while Eq. (6) leads to  $\sigma = (Dt)^{1/2+\theta}$ . Because  $\sigma$  grows at a rate slower than "normal" Fickian dispersion when  $\theta > 0$ , this behavior is referred to as subdiffusive.

The second approach assumes that a mass flux is proportional to a fractional derivative with respect to spatial and temporal coordinates. The mass balance equation yields:

$$\frac{\partial C}{\partial t} = \frac{\partial}{\partial x} \left( D_0 \partial_t^{1-\gamma} \frac{\partial^\beta C}{\partial x^\beta} \right) \quad (7)$$

where  $\beta$  and  $\gamma$  are the order of fractional derivatives, which can be set to non-integer values. Eq. (7) results in  $\sigma = (Dt)^{\gamma/1+\beta}$ .

Let us consider a fractured porous medium. At a microscopic level, we assume that a porous medium is constituted of tree-like fractures (pores) and in each of them a solute is mainly transported through the stem and a certain portion of the solute diffuses into the branching fractures. We assume that the surrounding pore medium is of fractal structure. The porosity is given by (Fomin et al., 2011):

$$\phi(r) = \phi_0 r^{d_f - n} \quad (8)$$

where  $\phi_0$  is a constant,  $r$  is the distance from a single pore,  $d_f$  is the fractal dimension of porosity, and  $n$  is the dimension of space. Using the diffusive mass flux in a single pore leads to temporal Caputo fractional derivatives, which accounts for the mass loss into the surrounding porous medium of fractal geometry. The time-fractional advection dispersion model (time fADE) with a temporal fractional derivative can be written as (Schumer et al., 2003; Fomin et al., 2011):

$$\frac{\partial C}{\partial \tau} + b \frac{\partial^\gamma C}{\partial \tau^\gamma} = \frac{1}{Pe} \frac{\partial^2 C}{\partial X^2} - \frac{\partial C}{\partial X} \quad (9)$$

where  $b$  is the retardation coefficient related to diffusion processes in the surrounding rocks, and  $b \frac{\partial^\gamma C}{\partial \tau^\gamma}$  is the Caputo fractional derivative with respect to time of order  $\gamma$  ( $0 < \gamma \leq 1$ ) defined in Samko (1993). When  $\gamma = 1$ , the time fADE model, Eq. (9), can be considered as the classical advection dispersion equation (ADE), which follows Fick's law.

Meerschaert et al. (2008) proposed the tempered anomalous diffusion model containing both the classical mass transport model and the temporal fractional derivative model as end members. The tempered stable model may be practically more attractive than the standard stable model in quantifying the late-time dynamics of mass transport. The tempered anomalous diffusion model for transient non-Fickian diffusion can be written as (Meerschaert et al., 2008):

$$\frac{\partial C}{\partial \tau} + b e^{-\lambda t} \frac{\partial^\gamma}{\partial \tau^\gamma} (e^{\lambda t} C) - b \lambda^\gamma C = \frac{1}{Pe} \frac{\partial^2 C}{\partial X^2} - \frac{\partial C}{\partial X} \quad (10)$$

where  $\lambda > 0$  is the truncation parameter in time.

Figure 5 shows the effects of model parameters: (a) the order of fractional derivative  $\gamma$  in the time fADE model (Eq. (9)) and (b) truncation parameter  $\lambda$  in the tempered anomalous diffusion model (Eq. (10)). The solutions by the time fADE model with  $\gamma = 0.1, 0.5$  appear decay at late time as power law (straight line on log-log plot)(Fig. 1 (a)). The solution of the classical ADE is also plotted, which exhibits a symmetric and exponential decline. The tempered anomalous diffusion model (Eq. (10)) reduces to the standard time fADE model (Eq. (9)) if  $\lambda \rightarrow 0$ , as seen in Fig. 1(b). Conversely, when  $\lambda \rightarrow 1$ , there is no power-law tail for arrival times larger than  $1/\lambda$ . The truncation parameter  $\lambda$  captures the transition from power-law to exponential decline for the breakthrough curve at late time. Zhang et al. (2014) discusses about a link between the specific model parameters in Eq. (10) and medium heterogeneity in alluvial settings. The relationship between the fractal dimension of porosity in Eq. (8), the model parameters in Eq. (10), and the fractal dimension of fracture length in Eq. (4) is the concern of this study.

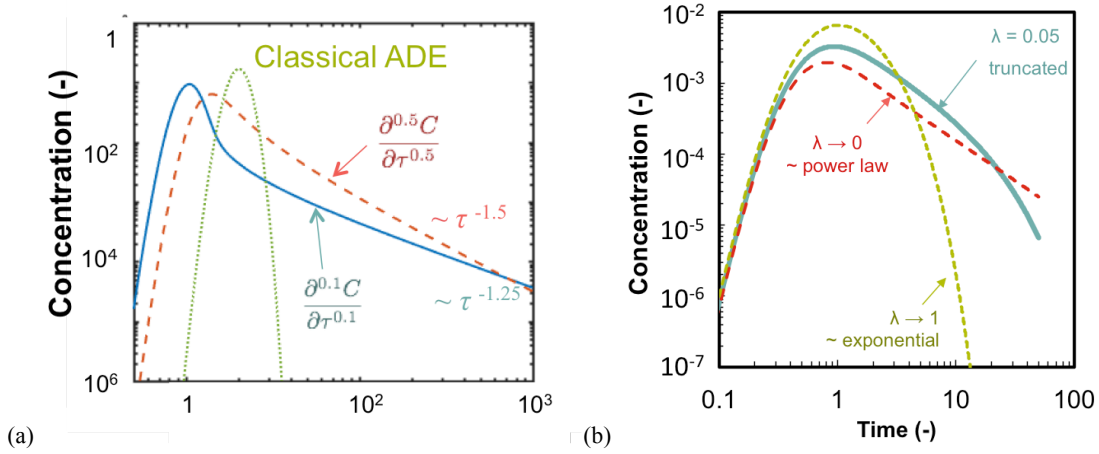


Figure 1: Effects of model parameters: (a) the order of fractional derivative  $\gamma$  in the time fADE model (Eq. (9)) and (b) truncation parameter  $\lambda$  in the tempered anomalous diffusion model (Eq. (10)) with  $\gamma=0.3$ .

### 3. PARTICLE TRACKING IN FRACTURE NETWORKS

#### 3.1 Method

We conducted tracer analyses using a particle tracking method to simulate fluid flow in a fracture network (Watanabe and Takahashi, 1995; Jing et al., 2000). The concept of particle tracking code generating tracer responses is illustrated in Fig. 2. Disc-shaped fractures are generated stochastically and randomly within a fracture generation area. The number of fractures is given by Eq. (4).

The fundamental relationship between fracture aperture and length has been debated. On the basis of theoretical fracture mechanics, some have argued aperture-to-length scaling should be linear. Vermilye and Scholz (1995) found that the geometry in a naturally formed extension can exhibit a linear scaling between length and displacement. This relationship implies that all fractures in a given population have the same driving stress regardless of fracture length. In contrast, some field observations indicate sublinear aperture-to-length scaling that is apparently inconsistent with the linear elastic fracture mechanics theory. Although the aperture-to-length scaling needs to be discussed, in this study, the fracture aperture is given to be proportional to its radius based on linear elastic fracture mechanics. The ratio of the fracture thickness to the radius is set to  $10^{-4}$  for numerical simulation.

The embedded fractures are converted to the "equivalent" permeability distribution (Fig. 2). The permeabilities on interfaces of grid cells in each axis direction;  $K_x$ ,  $K_y$ ,  $K_z$ , are given by the following equations:

$$K_x = \sum_j \frac{\eta_j^2 \eta_j L_j}{12 A_x}, K_y = \sum_j \frac{\eta_j^2 \eta_j L_j}{12 A_y}, K_z = \sum_j \frac{\eta_j^2 \eta_j L_j}{12 A_z}, \quad (11)$$

where  $A_x$ ,  $A_y$ ,  $A_z$  are the areas of grid cell interfaces orthogonal to the  $x$ ,  $y$ , and  $z$  axis, respectively. All fractures crossing at each interface of grid cell are numbered in  $j$ . The aperture and the length of the fracture intersecting the interface of grid cells are written as  $\eta_j$  and  $L_j$ . The equivalent permeabilities are used to calculate the flow rate at each interface of grid cells in each axis direction by using the following Darcy's law:

$$Q_x = A_x \frac{K_x}{\mu} \frac{\Delta P}{\Delta x}; Q_y = A_y \frac{K_y}{\mu} \frac{\Delta P}{\Delta y}; Q_z = A_z \frac{K_z}{\mu} \frac{\Delta P}{\Delta z}, \quad (12)$$

where  $\Delta P/\Delta x$  is pressure gradient, and  $\mu$  is the viscosity of water. In this study, incompressible, single-phase flows were considered. The density of rock and water, the viscosity of water, and the porosity are assumed constant. Constant pressure conditions are given at the upstream and the downstream boundaries. No flow conditions are used at the side boundaries. Steady-state flow solutions are solved numerically by relaxation methods using an iterative multigrid algorithm.

A particle-tracking code was used to calculate simulate tracer migration. In total, 10,000 tracer particles are injected as a pulse from the upstream boundary. A tracer particle migrates from a grid cell to its adjacent grid cell until the particle reaches the downstream boundary. The travel direction of tracers is determined by probability that depend on the magnitude of the flow rate given by Eq. (12). A plot of the number of tracers at the downstream boundary over time is used as a tracer response curve. The simulation parameters used for FRACSIM-3D are listed in Table 1.

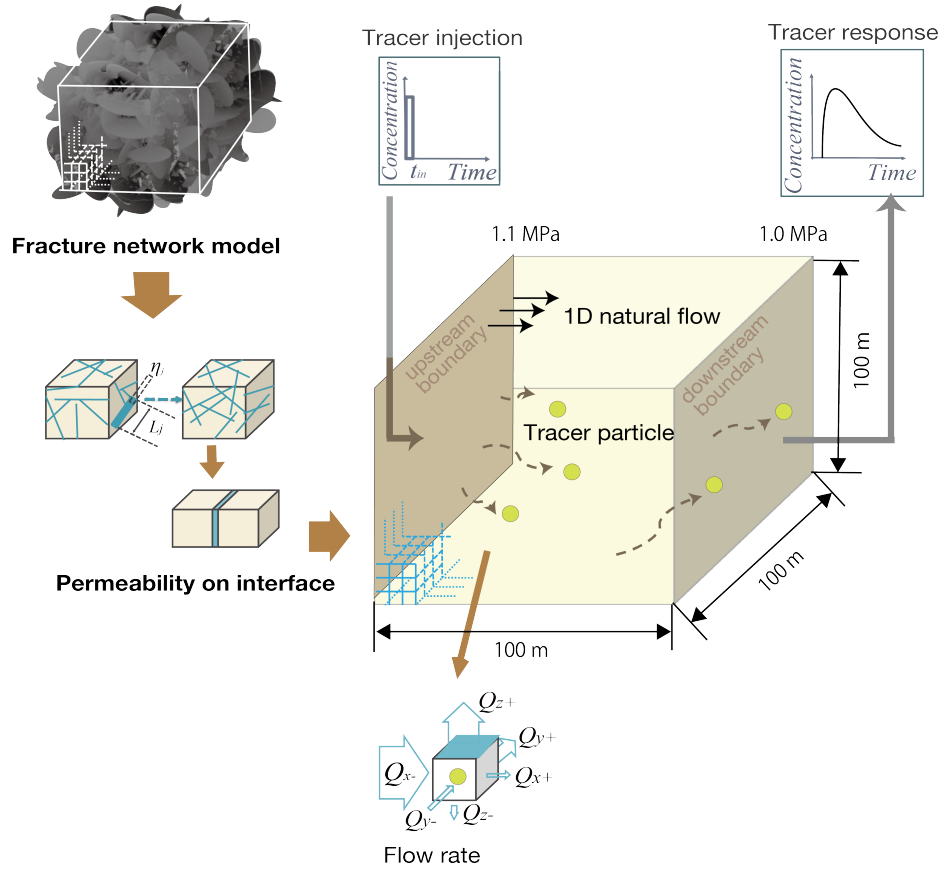


Figure 2: Schematic of particle tracking method.

Table 1: Numerical properties used in the particle tracking method.

Parameter	Value
Domain [m <sup>3</sup> ]	100 × 100 × 100
Number of grid cells [grids]	100 × 100 × 100
Fracture radius $r$ [m]	0.5 - 25
The ratio of fracture aperture to radius	$1.0 \times 10^{-4}$
Fractal dimension of fracture radius $D_R$	2.0 - 3.0
Fracture density [m <sup>-1</sup> ]	0.7, 1.5
Pressure difference between upstream and downstream boundaries [MPa]	0.1
Viscosity of water $\mu$ [Pa · s] at 25°C	$8.9 \times 10^{-4}$
Number of tracer particles [Particles]	10000

### 3.2 Numerical simulation results

We generated 100 fracture network models where the fracture radius is set to a constant ( $r = 1.0$  [m]) (Model U). Fractures are spatially randomly placed. An example of fracture cluster of Model U and the histogram of the permeability distribution are shown in Figs. 3(a) and 3(b). Fracture density is  $1.5 \text{ m}^{-1}$ . The average values calculated by using 100 fracture network models are plotted in the histogram of

permeability in Fig. 3(b). The model U shows that may small fracture distributed evenly. As seen in Fig 3(b), most values of permeability (more than 95%) are within the range between  $10^{-13}$  and  $10^{-14}$  m<sup>2</sup>.

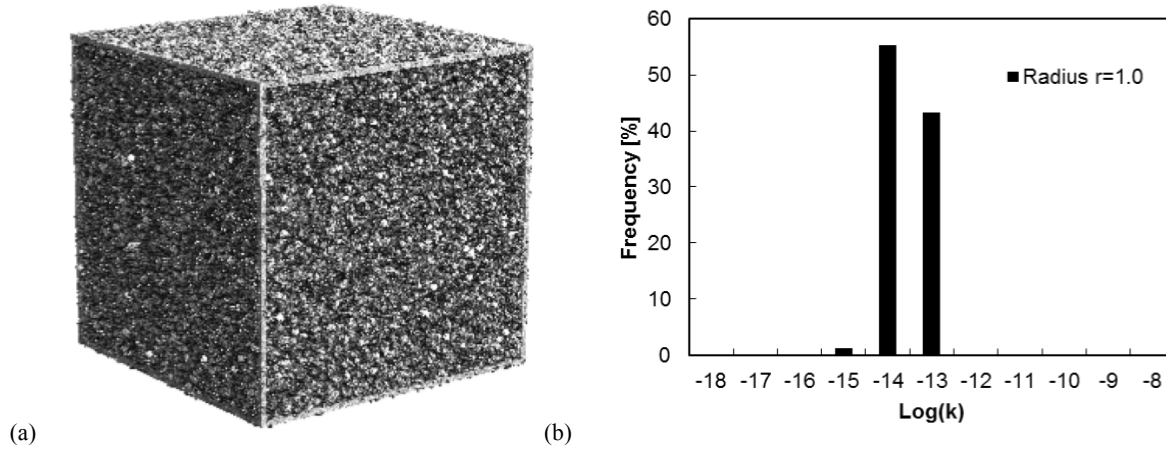


**Figure 3: (a) Illustration of fracture network of Model U with  $r = 1.0$  [m] and (b) the histogram of permeability distribution. Fracture density is  $1.5 \text{ m}^{-1}$ .**

Subsequently, 100 fracture network models with variable fracture radius (Eq. (4)) were generated, which is called Model  $D_R$ . The fracture radius was varied within the range of 0.5 m - 25 m. The minimum fracture radius (= 0.5 m) is equivalent to the half size of the grid cells. A fracture is detected to calculate permeability given by Eq. (11) when the fracture crosses the interfaces between grid cells. If a fracture is placed within a grid cell completely, the fracture is neglected. Thus, the minimum fracture radius is set to the half of grid cells. The maximum fracture radius (= 25 m) is the quarter of the calculation area. There is no fracture directly connecting the upstream and the downstream boundaries. The fractal dimension  $D_R$  given in Eq. (4) is set to a range between 2.0 and 3.0 because two-dimensional disc-shaped fractures are distributed in the three-dimensional region. The fracture density for different  $D_R$  is adjusted to be constant by using the parameter  $C$ . The fracture density (number of fractures per meter) is obtained by counting the number of fractures intersecting a line and by averaging the number of fractures at nine lines. The fracture density with respect to the number per meter shows similar trends with the area of fracture surface per cube. After evaluating the fracture density, the total number of fractures  $N_R$  in Eq. (4) is determined.

Effects of the fractal dimension  $D_R$  on Model  $D_R$  are shown in Fig. 4. Fracture densities for different  $D_R$  are same ( $1.5 \text{ m}^{-1}$ ). As seen in Figs. 4(a)-(c), the network with smaller  $D_R$  contains many large fractures. In contrast, a fracture network with greater  $D_R$  has high proportion of small fractures. This is consistent with other studies (Le Garzic et al., 2011). Figure 4(d) illustrates the histogram of permeability distribution for Model  $D_R$ . The permeability distribution for Model  $D_R$  has a wide range between  $10^{-16}$  and  $10^{-11}$  m<sup>2</sup>. The result obviously differs from the permeability for Model U (Fig. 3(b)). In Model  $D_R$ , higher permeability ( $k = 10^{-10}$  [m<sup>2</sup>]) is dominant for  $D_R = 2.0$ , while lower permeability ( $k = 10^{-13}$  [m<sup>2</sup>]) is dominant for  $D_R = 2.5$  and  $D_R = 3.0$ . The number of large fractures decreases with increase in  $D_R$ , which leads to decrease the overall permeability. When  $D_R = 3.0$ , the peak of permeability distribution is between  $10^{-13}$  and  $10^{-14}$  m<sup>2</sup>. The peak value is higher than that for smaller  $D_R$ . This indicates that  $D_R$  of 3.0 has less variance of permeability distribution than smaller  $D_R$ .

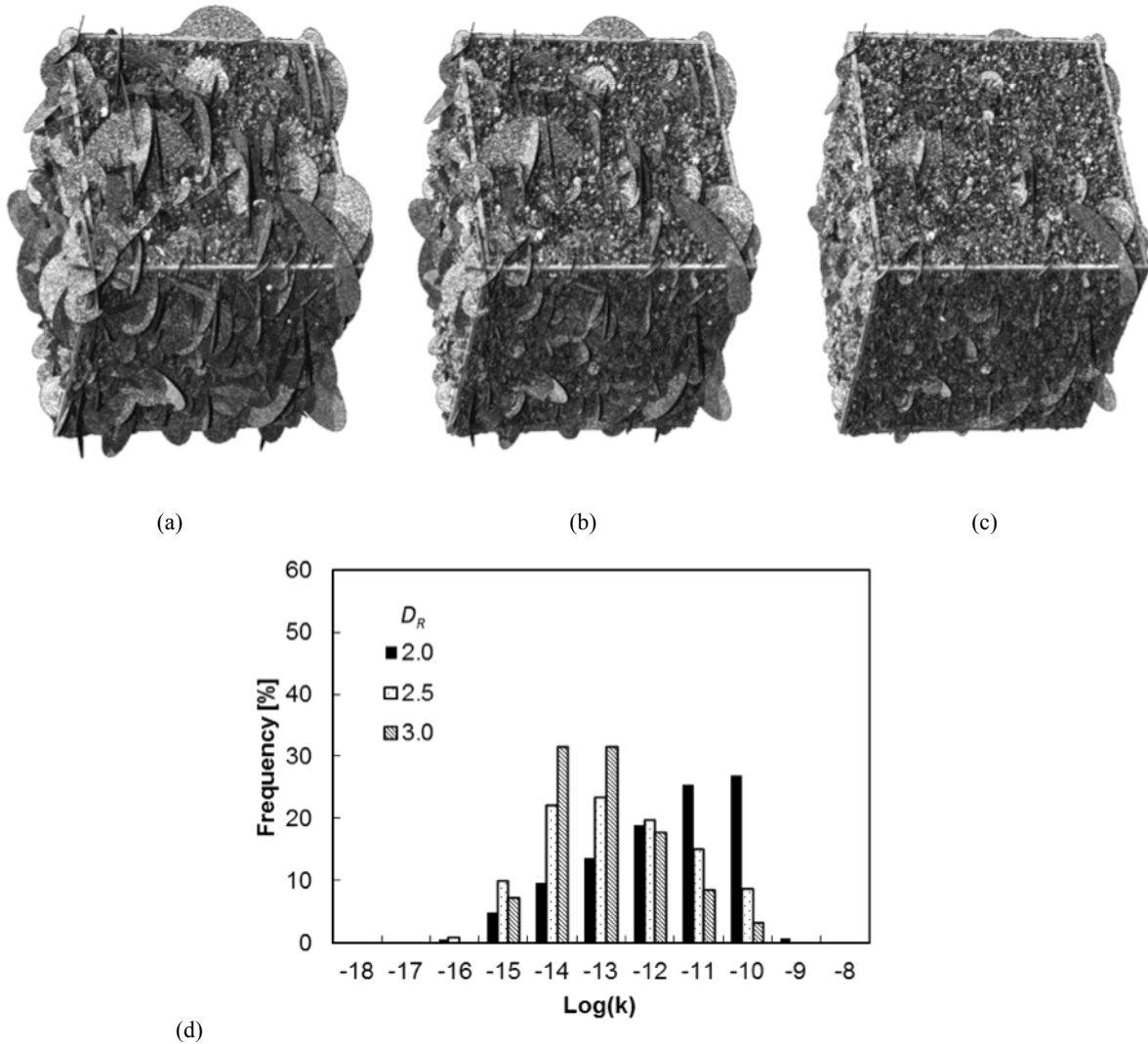


**Figure 4: (a) Illustration of fracture network of Model  $D_R$  : (a) 2.0, (b) 2.5, and (b) 3.0 and (d) the histograms of permeability distribution. Fracture density is  $1.5 \text{ m}^{-1}$ .**

A box-counting method has been used to estimate fractal dimension of box-counting ( $D_{box}$ ) in field data (Main, 1990). We evaluated  $D_{box}$  for different  $D_R$  by using a three-dimensional box-counting algorithm. The calculation domain is divided into cubes, and the number of cubes including a part of the object is counted. As the length of the divided cube varies by a factor of  $2^n$  ( $n = 0, \pm 1, \pm 2, \dots$ ), a logarithm plot of the length and the number of cubes gives the value of  $D_{box}$ . Using Model  $D_R$ , we observed that the  $D_{box}$  has a positive correlation to the  $D_R$ . The linear approximation for the fracture density of  $0.7 \text{ m}^{-1}$  is given as  $D_{box} = 0.106 D_r + 2.579$  where the coefficient of determination  $R^2 = 0.97943$ . The value of  $D_{box}$  can be used to evaluate spatial distributions of fractures. When  $D_{box}$  is 3.0, all boxes are occupied because of using cubic boxes. Then, the distribution of disk-shaped fractures is spatially even in the three-dimensional area. In contrast, when  $D_{box}$  is 2.0, the disk-shaped fractures are distributed on a two-dimensional plane. The positive correlation between  $D_{box}$  and  $D_r$  suggests that a greater  $D_R$  leads to a network where fractures are spatially evenly distributed, while a lower  $D_R$  results in unevenly distribution of fractures.

The results for Model U and Model  $D_R$  are plotted in Fig. 5. The solution of the classical ADE model following Fick's law is also presented in Fig. 4. Fracture densities are  $1.5 \text{ m}^{-1}$  in both models. Model U yields a sharp peak, which can be reproduced by the classical ADE model. On the other hand, the tracer response for Model  $D_R$  exhibits a long tail. Because the classical ADE model is in disagreement with the curve, the tracer response is called non-Fickian (Hatano and Hatano, 1998; L evy and Berkowitz, 2003; Benson et al., 2000). Unlike Model U, Model  $D_R$  distributes fractures with several lengths and several apertures due to the fractal of the fracture length. The variance of permeability for Model  $D_R$  is greater than that for Model U, which can be compared in Figs. 2 and 3. Because of this wide range of permeability for Model  $D_R$ , some tracers move through preference paths (larger fractures) and some tracers migrates into less permeable zones (smaller fractures). The tailing in the tracer response shown in Fig. 4 is caused by such retardation of tracers. Therefore, it is said that the fractal nature of the fracture length is one of factors that non-Fickian behavior is caused.

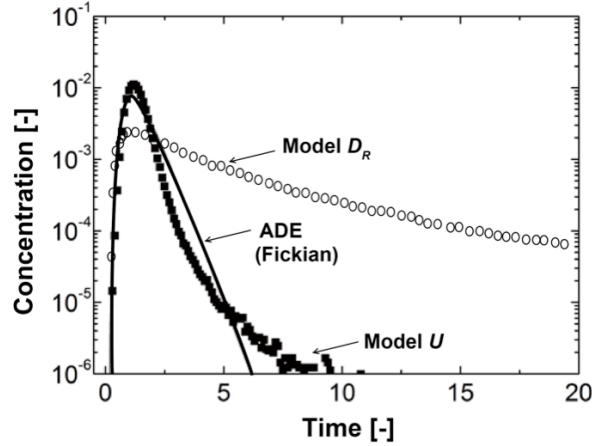


**Figure 5: Simulated tracer curves for Model U and Model  $D_R$  and fitted curve of the ADE. Fracture density is  $1.5 \text{ m}^{-1}$ .**

Tracer responses with different  $D_R$  are plotted in Fig. 6. The fracture densities for all models are  $1.5 \text{ m}^{-1}$ . The tracer response for  $D_R = 2.0$  exhibits a sharper peak at early time, while the peaks delay and become wider when  $D_R$  increases. As discussed above, model with smaller  $D_R$  has greater amount of large fractures, which creates preference paths. Thus, the sharper peak with  $D_R = 2.0$  is caused by tracer migration through the preference paths. In contrast, models with greater  $D_R$  decrease in the number of larger fractures. Instead of large fractures, the greater number of smaller fractures is distributed. Thus, the peak is delayed with increase in  $D_R$ . These results suggest that tracer response has some information of fractal dimension of fracture length and can be used to estimate the value of  $D_R$ . Because fractal dimension has been determined by using outcrop data in previous research, this estimation can provide new sights and be useful to understand fracture structure inside reservoirs.

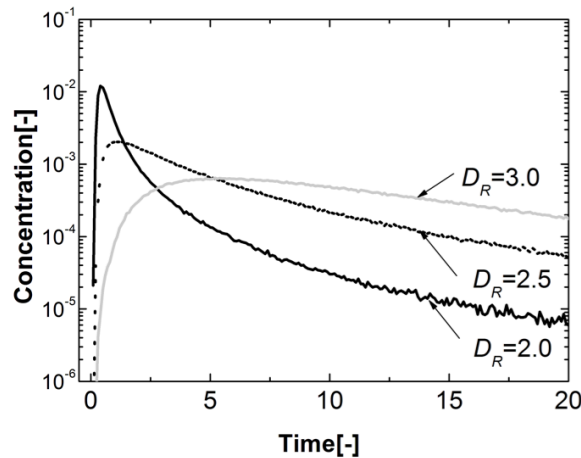


**Figure 6: Simulated tracer curves for Model  $D_R$  with different  $D_R$ . Fracture density is  $1.5 \text{ m}^{-1}$ .**

#### 4. FLOW EXPERIMENT

##### 4.1 Creating fracture networks for 3D printer

Fracture network models were created using a 3D CAD modeler called “OpenSCAD”. Each model was generated in the same manner as introduced in the previous session. A cluster of the fractures is shown in Fig. 7(a). The maximum radius was set to a quarter of the sample length in order to prevent the fracture from penetrating through the sample. The minimum radius is determined by the resolution of the 3D printer. After the cluster of the fracture network is created, a solid cylinder is subtracted by the cluster, leaving the cylinder with the hollow fracture network (Fig. 7(b)). The outside shell prevents water from exiting the sides (Fig. 7(c)). The inner and outer diameters of the model are 2.54 cm and 3.81 cm, respectively. The height of the model is 4 cm. The fracture properties to create fracture network model by OpenSCAD includes the position, radius, aperture, dip, and azimuth of each fracture. The simulation condition is listed in Table 2.

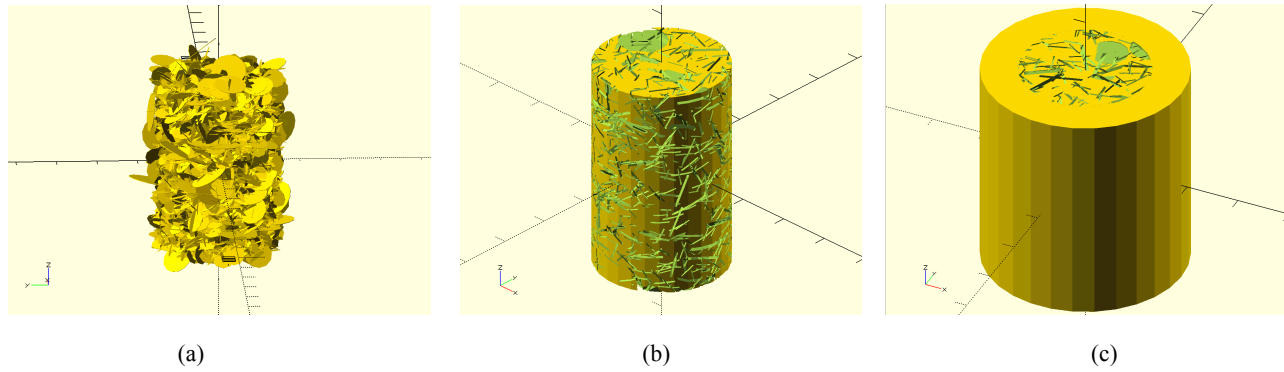


Figure 7: (a) A cluster of fracture network, (b) a solid cylinder after being subtracted, and (c) a model with cladding (ready to be printed).

Table 2: Parameters used to create models.

	Model 1	Model 2
Fractal dimension ( $D_R$ )	2	3
Constant of fracture density ( $C$ )	500	1150
Aperture ratio (thickness/radius)	0.125	0.125
Minimum fracture radius	1.6 mm	1.6 mm
Maximum fracture radius	8 mm	8 mm

In order to carry out a feasibility experiment, the median permeability was determined to  $2.3 \times 10^{-11} \text{ m}^2$  for both models. A computer program was used to find the average permeability. The program discretizes the simulation area into cubic blocks and calculates the interface permeability on each block by using the cubic law. The median permeability is compared to find an appropriate value of parameter  $C$  in Eq. (3) as shown in Fig. 8.

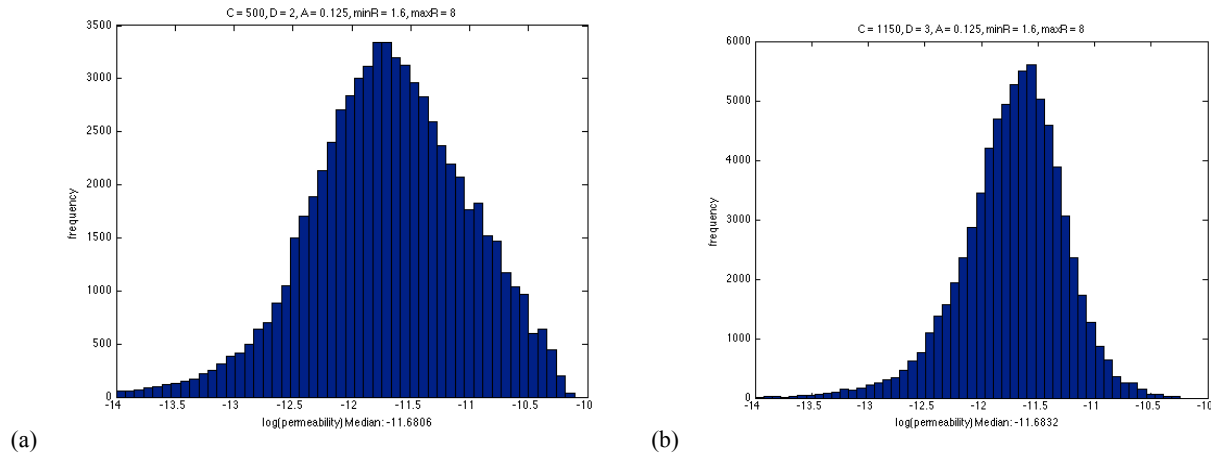
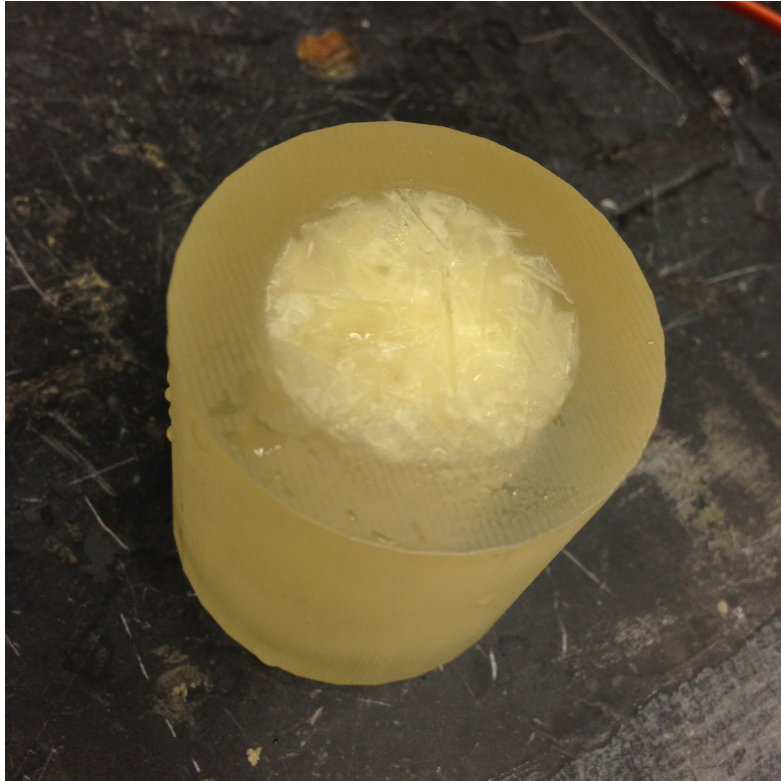


Figure 8: Permeability distribution of models for (a)  $D_R = 2.0$  and of (b)  $D_R = 3.0$ .

The file format STL contains the data of the triangles that form the 3D models, which are then sent to 3D printer. To create the models, OpenSCAD was used to compile and render the codes into STL file. For a trial, there were two models printed in this project, a model with  $D_R$  of 2.0 and one with  $D_R$  of 3.0.

We used a 3D printer (VisiJet ® EX200 Plastic Material for 3-D Modeling, 3D Systems) at the Stanford 3-Dimensional Printing Facility (3D). The properties of the materials used are listed in Table 3. The resolution of the printer is 16 micron. Unique aspects of the printing technology allow feather-weight thin structures. The unique printing technology results in truly solid, nonporous parts. The 3D printer prints a model consisting of plastic (UV Curable Acrylic Plastic) and supporting wax. The supporting wax is required for the 3D printer to print hanging parts. Figure 9 shows a 3D printed sample. After printing, the models were immersed in an ultrasonic oil bath in which

the oil was heated to melt the wax. To make sure that the wax was removed as much as possible, the models were submerged in hot water at 70 °C and shaken for approximately an hour so that the wax melted and floated up through the holes (Fig. 10). Then, the models were put in a system that a pump pumps ethanol through the fracture network overnight so that ethanol dissolves the remaining wax (Fig. 11).



**Figure 9: A 3D-printed model.**

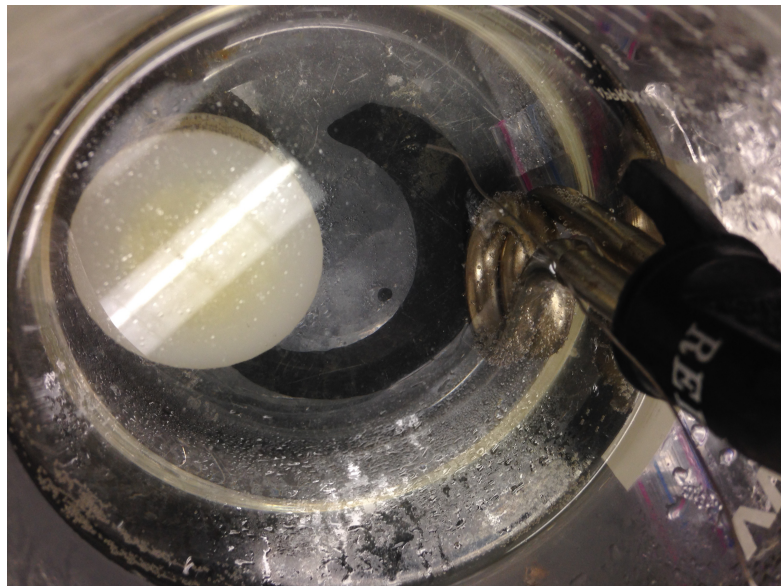


**Figure 10: A model being heated.**

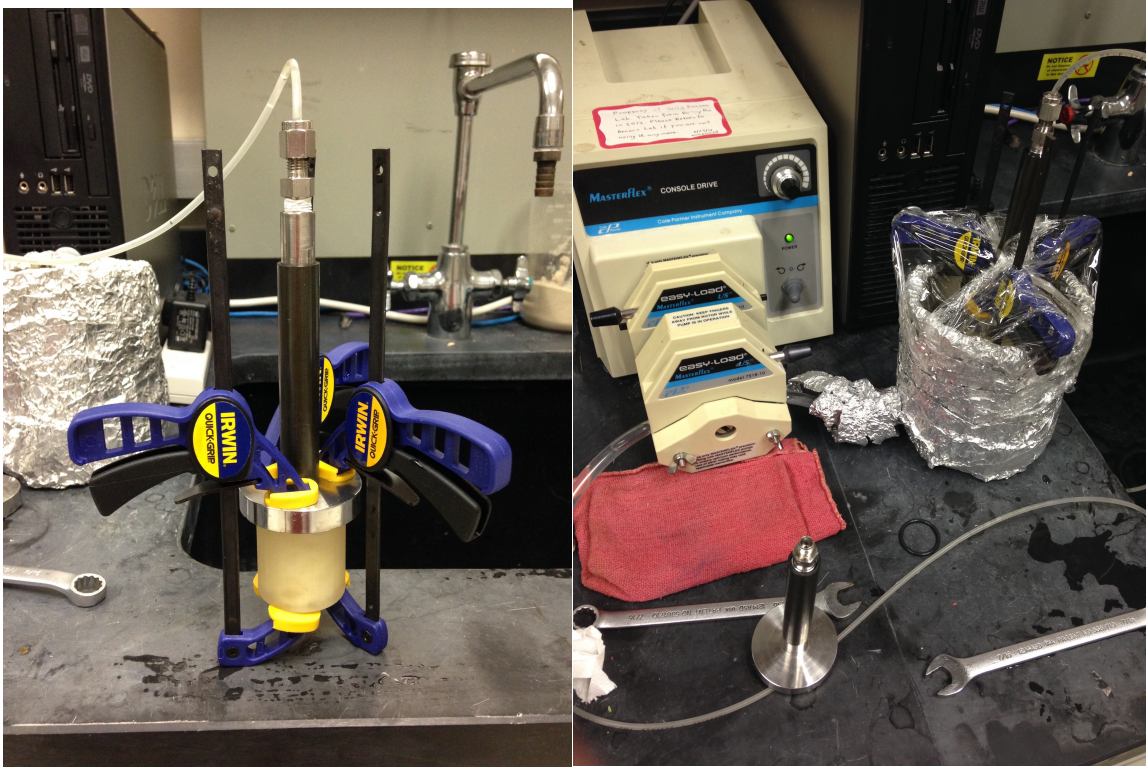


**Figure 11: The apparatus in which ethanol is injected into the model and circulated by a pump.**

**Table 3: Properties of printing material.**

Properties	Value
Composition	UV Curable Acrylic Plastic
Density at 80 °C (liquid) [g/cm <sup>3</sup> ]	1.02
Tensile strength [MPa]	42.2
Tensile Modulus [MPa]	1283
Printer resolution [ $\mu\text{m}$ ]	16

After the wax had been removed, the printed models were flooded with water with sodium chloride as a tracer. Figure 12 shows the configuration of the flow test. First, the water is injected into the models by hydraulic head difference for about half an hour to saturate the fractures with water. The injected water is distributed at the inlet of the fracture network model at the inlet using a “spider connection” that has radial drain channels. The elevation of the water source is 1 meter, so the pressure at the inlet is about  $10^4$  Pa. Resistivity and mass of the water that flows out were measured over time at the outlet during the test by using a DE-6000 LCR meter by IET and a Sartorius digital scale. The spider connection was used at the outlet as well. Once the resistivity had stabilized, 2 milliliters of salt water were injected.

The LCR meter in this experiment uses alternating current to measure the resistivity. Therefore, in order to obtain the real resistivity of the salt water, the measurement needed to be made with different frequencies so that the impedance due to capacitance can be eliminated. Once the true resistivity is obtained, it can be inverted to conductivity. The conductivity data were converted to concentration by assuming that concentration has a linear relationship with conductivity.

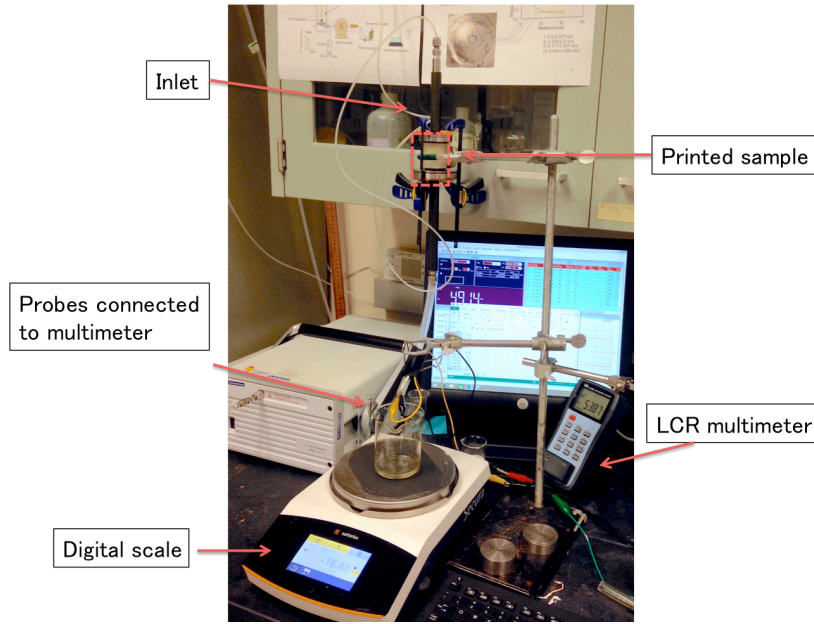


Figure 12: The configuration of the experimental apparatus, distilled and salt water on the shelf are not shown.

#### 4.2 Experimental results

Tracer responses using the 3D printed samples are shown in Figure 13. The tracer for  $D_R = 2.0$  reached the outlet faster, and the peak is sharper than the response for  $D_R = 3.0$ . These results are consistent with the results discussed for the numerical simulation in previous section. The peaks appear at 26 sec and 55 sec for  $D_R$  of 2.0 and 3.0, respectively. The estimated velocity for this sample is  $8.71 \times 10^{-4}$  m/s and the estimated travel time between the inlet and the outlet is 45.9 sec based on the Darcy’s law. Note that the average permeability of samples of  $2.3 \times 10^{-11}$  m<sup>2</sup>, the hydraulic head difference of 1.0 m, and the water viscosity of  $8.90 \times 10^{-4}$  Pa·s at 25 °C. The peaks are almost same order as the estimated travel time.

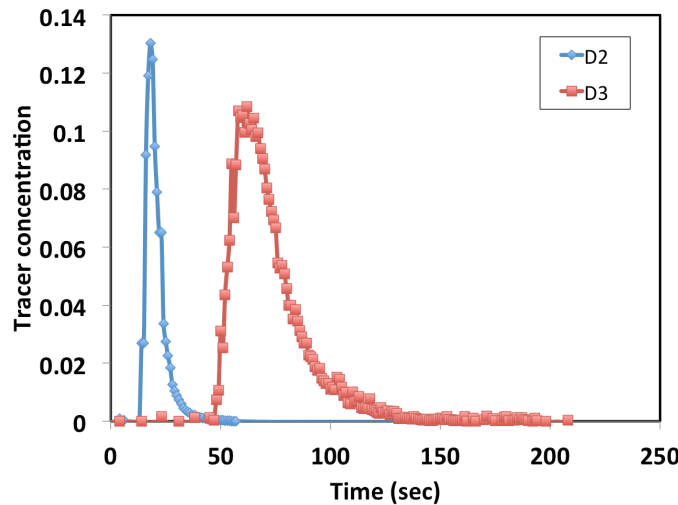


Figure 13: Tracer response results using 3D printed samples.

#### 6. DISCUSSION

Some of the findings from numerical simulation are summarized in Table 4. The fracture densities for different  $D_R$  were unified in the numerical simulation, while the median permeabilities were unified in the experiment. Even so, the experimental results are consistent with numerical simulation results. However, the frequency of the permeability distribution, shown in Figs. 4(b) and 8, exhibited a difference in the case of  $D_R = 2.0$ . The histogram of permeability for the experiment distributes almost symmetrically, while that for numerical simulation is asymmetric. Additionally, the experimental results did not show heavy tails as in the numerical simulation results. These results may depend on the value of fracture density or permeability, the size of fractures, the size of system, and other conditions. We created the fracture network with 4-centimeter height and 1-inch diameter. The radius of distributed fractures was in a range between 1.6 mm and 8 mm, which is a shallower range than in the numerical simulation (0.5 m – 25 m). Further research will conduct experiments with a wider range of fracture length and investigate carefully the effect of fracture density on permeability.

**Table 4: Summary of effect of fractal dimension  $D_R$  on tracer response.**

$D_R$	2.0	3.0
Fracture		
Dominant fracture size	Large	Small
Variance of permeability	Large	Small
Spatial distribution	Unevenly distributed	Evenly distributed
Tracer		
Peak time	Early	Late
Peak shape	Sharp	Wide

One of the challenges in this experiment were the limitations of the 3D printer: the limited resolution of the 3D printer and the difficulty of removing the wax. Although the published resolution value of the printer is 0.16  $\mu\text{m}$ , it is not expected to obtain such a high accuracy in the inside of the sample due to complex shapes. As an alternative, using larger size of samples is desirable in future research. Ethanol was used to dissolve the remaining wax in this study. Another way to dissolve wax is to use hexane or other appropriate alkane (Song et al., 2014). Then, the model could be flushed in a sequence of toluene, isopropyl alcohol, and water.

The main goal of this research was to characterize fracture network based on fractal geometry with some cutoffs, by using tracer responses. Truncated models including the tempered anomalous diffusion model (Meershaert et al., 2008) (Eq. (10)) might help provide description of truncated mass transport beyond the fractal theory and are expected to contribute to broader application. In the next step, we will analyze tracer responses by using the truncated model to find the relationships between the model constitutive parameters and the fracture properties (i.e., fractal dimension, maximum and minimum size, aperture).

## 7. CONCLUSIONS

We studied mass transport in a fracture network where fracture radius are given by a power law with maximum and minimum limits. In order to investigate the effects of fractal dimension of fracture length on mass transport, particle tracking simulations and laboratory experiments were conducted. A fracture network model with constant fracture radius generated a tracer response that was similar to Fickian behavior. In contrast, a fracture network where the fracture radius was given by a power law exhibited a significant long tail. The fractal nature of the fracture length was considered one of the factors causing this non-Fickian behavior. For the laboratory flow experiment, samples of fracture networks were created by a 3D printer. Due to the limited resolution of the 3D printer and the sample size, the model only covered a limited range of fracture sizes. Despite the limitation, the experimental results were consistent with the numerical simulation results. This suggests that the tracer response can be used to provide the information of the porous media in terms of fractal dimension. Further investigation needs the use of larger fracture network models. It is also necessary to solve the problem of wax residue.

## ACKNOWLEDGEMENTS

This work was supported by the Japan Society for the Promotion of Science, under JSPS Postdoctoral Fellowships for Research Abroad (H26-416) and 2015 Stanford Earth Summer Undergraduate Research Program (SESUR), whose supports are gratefully acknowledged.

## REFERENCES

- Abbas, S., Benchohra, M., N'Guérékata, G.M., 2012. Topics in fractional differential equations.
- Bear J., 1972. Dynamics of Fluids in Porous Media. New York: American Elsevier.
- Benson, D. a. D.A., Wheatcraft, S.W.S.W., Meerschaert, M.M., 2000. Application of a fractional advection-dispersion equation. Water Resour. Res. 36, 1403–1412. doi:10.1029/2000WR900031
- Benson, D.A., Schumer, R., Meerschaert, M.M., Wheatcraft, S., 2001. Fractional dispersion, Lévy motion, and the MADE tracer tests. Transp. Porous Media 42, 211–240.
- Benson, D.A., Wheatcraft, S.W., Meerschaert, M.M., 2000. The fractional-order governing equation of Lévy motion. Water Resour. Res. 36, 1413–1423.
- Berkowitz, B., Bour, O., Davy, P., Odling, N., 2000. Scaling of fracture connectivity in geological formations. Geophys. Res. Lett. 27, 2061–2064.
- Berkowitz, B., Cortis, A., Dentz, M., Scher, H., 2006. Modeling non-fickian transport in geological formations as a continuous time random walk. Rev. Geophys. 44, 1–49. doi:10.1029/2005RG000178

- Bonnet, E., Bour, O., Odling, N.E., Davy, P., Main, I., Cowie, P., Berkowitz, B., P. Davy, Main, I., Cowie, P., Berkowitz, B., 2001. Scaling of fracture systems in geological media. *Rev. Geophys.* 39, 347–383.
- Bour, O., Davy, P., 1997. Connectivity of random fault networks following a power law fault length distribution. *Water Resour. Res.* 33, 1567–1583.
- Cartea, Á., Del-Castillo-Negrete, D., 2007. Fluid limit of the continuous-time random walk with general Lévy jump distribution functions. *Phys. Rev. E* 76, 041105. doi:10.1103/PhysRevE.76.041105
- Castaing, C., Halawani, M.A., Gervais, F., Chilés, J.P., Genter, A., Bourguin, B., Ouillon, G., Brosse, J.M., Martin, P., Genna, A., Janjou, D., 1996. Scaling relationships in intraplate fracture systems related to Red Sea rifting. *Tectonophysics* 261, 291 – 314. doi:10.1016/0040-1951(95)00177-8
- Diethelm, K., Freed, A.D., 1999. On the solution of nonlinear fractional order differential equations used in the modeling of viscoplasticity, in *Scientific Computing in Chemical Engineering II-Computational Fluid Dynamics, Reaction Engineering and Molecular Properties*, Springer, Heidelberg, 217–224.
- Einstein, H.H., Baecher, B.G., 1983. Probabilistic and Statistical Methods in Engineering Geology Specific Methods and Examples Part I: Exploration. *Rock Mech. Rock Eng.* 16, 39–72.
- Falconer, K., 1990. *Fractal Geometry: Mathematical Foundations and Applications*, John Wiley, New York.
- Feder, J., 1988. *Fractals*, Plenum, New York.
- Giona, M., Roman, H.E., 1992. Fractional diffusion equation on fractals: one-dimensional case and asymptotic behaviour. *J. Phys. A. Math. Gen.* 25, 2093 – 2105.
- Gustafson, G., Fransson, Å., 2005. The use of the Pareto distribution for fracture transmissivity assessment. *Hydrogeol. J.* 14, 15–20. doi:10.1007/s10040-005-0440-y
- Haggerty, R., Gorelick, S.M., 1995. Multiple-rate mass transfer for modeling diffusion and surface reactions in media with pore-scale heterogeneity. *Water Resour. Res.* 31, 2383–2400.
- Haggerty, R., Wondzell, S.M., Johnson, M.A., 2002. Power-law residence time distribution in the hyporheic zone of a 2nd-order mountain stream. *Geophys. Res. Lett.* 29, 1640.
- Hatano, Y., Hatano, N., 1998. Dispersive transport of ions in column experiments: An explanation of long-tailed profiles. *Water Resour. Res.* 34, 1027–1033.
- Hilfer, R., 2000. in *Applications of Fractional Calculus in Physics*, World Scientific, Singapore.
- Huang, G., Huang, Q., Zhan, H., 2006. Evidence of one-dimensional scale-dependent fractional advection-dispersion. *J. Contam. Hydrol.* 85, 53–71. doi:10.1016/j.jconhyd.2005.12.007
- Jing, Z., Willis-Richards, J., Watanabe, K., Hashida, T., 2000. A three-dimensional stochastic rock mechanics model of engineered geothermal systems in fractured crystalline rock. *J. Geophys. Res.* doi:10.1029/2000JB900202
- Le Garzic, E., de L'Hamaide, T., Diraison, M., Géraud, Y., Sausse, J., de Urreiztieta, M., Hauville, B., Champanhet, J.-M., 2011. Scaling and geometric properties of extensional fracture systems in the proterozoic basement of Yemen. *Tectonic interpretation and fluid flow implications. J. Struct. Geol.* 33, 519–536. doi:10.1016/j.jsg.2011.01.012
- Levy, M., Berkowitz, B., 2003. Measurement and analysis of non-Fickian dispersion in heterogeneous porous media. *J. Contam. Hydrol.* 64, 203–26. doi:10.1016/S0169-7722(02)00204-8
- Mainardi, F., 1997. Fractional calculus: Some basic problems in continuum and statistical mechanics, in *Fractals and Fractional Calculus in Continuum Mechanics*, Springer Verlag, Wien, 291–348.
- Mantegna, R.N., Stanley, H.E., 1994. Stochastic process with ultraslow convergence to a Gaussian: The truncated Lévy flight. *Phys. Rev. Lett.* 73, 2946 – 2949.
- Magin, R., 2006. in *Fractional Calculus in Bioengineering*, Begell House Publishers, Redding.
- Meerschaert, M.M., Zhang, Y., Baeumer, B., 2008. Tempered anomalous diffusion in heterogeneous systems. *Geophys. Res. Lett.* 35, 1–5. doi:10.1029/2008GL034899
- Metzler, F., Schick, W., Kilian, H.G., Nonnenmacher, T.F., 1995. Relaxation in filled polymers: A fractional calculus approach. *J. Chem. Phys.* 103, 7180–7186.
- Neuman, S.P., 2005. Trends, prospects and challenges in quantifying flow and transport through fractured rocks. *Hydrogeol. J.* 13, 124–147. doi:10.1007/s10040-004-0397-2
- O'Shaughnessy, B., Procaccia, I., 1985. Diffusion on fractals. *Phys. Rev. A* 32, 3073–3083. doi:10.1103/PhysRevA.32.3073
- Odling, N.E., 1997. Scaling and connectivity of joint systems in sandstones from western Norway. *J. Struct. Geol.* 19, 1257 – 1271.

- Odling, N.E., Gillespie, P., Bourguine, B., Castaing, C., Chilés, J.-P., Christensen, N.P., Fillion, E., Genter, A., Olsen, C., Thrane, L., Trice, R., Aarseth, E., Walsh, J.J., Watterson, J., 1999. Variations in fracture system geometry and their implications for fluid flow in fractured hydrocarbon reservoirs. *Pet. Geosci.* 5, 373 – 384.
- Rosiński, J., 2007. Tempering stable processes. *Stoch. Process. their Appl.* 117, 677–707. doi:10.1016/j.spa.2006.10.003
- Samko, SG, Kilbas, AA, Marichev, OI. *Fractional integrals and derivatives: theory and applications*. London: Gordon and Breach; 1993.
- Schumer, R., Benson, D. a., Meerschaert, M.M., Baeumer, B., 2003. Fractal mobile/immobile solute transport. *Water Resour. Res.* 39. doi:10.1029/2003WR002141
- Segall, P., Pollard, D.D., 1983. Joint formation in granitic rock of the Sierra Nevada. *Geol. Soc. Am. Bull.* 94, 563 – 575.
- Sheng, H., Chen, Y., Qiu, T., 2011. In *Fractional Processes and Fractional-order Signal Processing: Techniques and Applications*, Springer-Verlag, London.
- Shlesinger, M.F., Zaslavsky, G.M., Klafter, J., 1993. Strange kinetics. *Nature* 363, 31 – 37.
- Song, W., Haas, T. W., Fadaeia, H. Sinton, D., 2014. Chip-off-the-old-rock: the study of reservoir-relevant geological processes with real-rock micromodels, *Lab Chip*, 14, 4382-4390.
- Tarasov, V.E., in *Fractional dynamics: Application of Fractional Calculus to Dynamics of Particles, Fields and Media*, Springer, Heidelberg, 2010.
- Vermilye, J.M., Scholz, C.H., 1995. Relation between vein length and aperture. *J. Struct. Geol.* 17, 423–434. doi:10.1016/0191-8141(94)00058-8
- Vicsek, T., *Fractal Growth Phenomena*, 488 pp., World Sci., River Edge, N. J., 1992.
- Watanabe, K., Takahashi, H., 1995. Fractal geometry characterization of geothermal reservoir fracture networks. *J. Geophys. Res.* doi:10.1029/94JB02167
- Zhang, Y., Benson, D. a. D.A., Reeves, D.M.D.M., 2009. Time and space nonlocalities underlying fractional-derivative models: Distinction and literature review of field applications. *Adv. Water Resour.* 32, 561–581. doi:10.1016/j.advwatres.2009.01.008